



## 1 **1. Introduction**

2       Advanced manufacturing techniques such as 3D Laser Foil Printing (LFP) and  
3 Laser Circular Oscillation Welding (LCOW) have garnered significant attention due to  
4 their potential to enhance the manufacturing quality and efficiency of aluminum alloy  
5 components. Laser Foil Printing (LFP) utilizes metal foils as raw materials and employs  
6 laser welding to progressively assemble them onto a substrate or pre-formed layers [1].  
7 This technique offers high precision in forming detailed cross-sectional profiles,  
8 effective heat conduction due to high cooling rates, and significantly reduces shrinkage  
9 cavities [2]. Subsequently, precise cutting is carried out to obtain the desired cross-  
10 sectional profile [3]. The thickness of the metal foils in the LFP process varies from  
11 tens to hundreds of micrometers. Furthermore, in the studies by Hung et al. [4-6], it can  
12 be observed that a distinctive feature of metal foils lies in their high cooling rate. This  
13 high cooling rate facilitates effective heat conduction during the melting process, thus  
14 aiding in the formation of fine-grained or even amorphous structures when needed.  
15 Additionally, due to the absence of significant volume shrinkage during both the  
16 melting and solidification phases, the occurrence of shrinkage cavities is substantially  
17 minimized overall.

18       However, LFP faces challenges such as aluminum's high reflectivity to lasers [7],  
19 which can cause spattering, burrs, and unstable keyholes, as well as high thermal  
20 conductivity, which can lead to hot cracks [8]. One of the most challenging issues in  
21 the laser welding of aluminum alloys is the high reflection of the surface. In [9]  
22 indicated that 92% – 98% of near-infrared laser beams are reflected by the surface of  
23 aluminum. On the other hand, in the realm of powder bed fused process in additive  
24 manufacturing, the issue of thermal cracking in materials like IN713LC and AA6061  
25 has been effectively addressed. Wang et al. [10] employed a method that combines

1 simulation models with experimental approaches to systematically pinpoint an  
2 optimized range of processing parameters. This zone enables the utilization of the  
3 optimal processing conditions for producing high-density ( $> 99.9\%$ ) components using  
4 IN713LC, thereby enhancing its relative density while minimizing microcracking.  
5 Chen et al. [11] also followed a similar approach to the former, methodically exploring  
6 the parameter optimization range. They introduced a small quantity of yttria-stabilized  
7 zirconia (YSZ) powder less than 2% in vol. into AA6061 raw material and employed  
8 L-PBF processing parameters that had been optimized to eliminate thermal cracking  
9 during the cooling phase. Consequently, they achieved an average density of 99.95% in  
10 the printed parts. Returning to the section on laser welding, in recent years, numerous  
11 studies have been focused on developing effective solutions to enhance the stability of  
12 keyholes and maximize the weldability of aluminum alloys. This has become possible  
13 through the introduction of techniques such as laser beam oscillation [12], power  
14 modulation [13], and beam shaping [14] serving as effective solutions to suppress the  
15 processing above defects. In the study by Wang et al. [15], it has been demonstrated  
16 that LCOW (Laser Circular Oscillation Welding) is an efficient and effective welding  
17 technique that seamlessly integrates the advantages of traditional laser welding with  
18 additional benefits.

19 By harnessing the exceptional energy density of the laser beam, LCOW can  
20 precisely control the shape and position of the molten pool during the welding process,  
21 leading to stable welds and significantly reducing defects like spatter and pores.  
22 Furthermore, in the study by Wang et al. [15], it is mentioned that the circular oscillation  
23 of the laser beam ensures precise and controlled heating, ensuring more uniform heat  
24 distribution and consistent metal melting. This enhances the overall stability of the  
25 welding process, ultimately contributing to the formation of high-quality welds with  
26 minimal defects. It is worth noting that Cen et al. and Zhang et al. [16, 17] have found

1 that a key mechanism in reducing cracks and pores in LCOW is to select higher  
2 scanning frequencies for processing parameters during laser welding. This results in the  
3 creation of wider and more stable keyholes, generating larger and shallower molten  
4 pools with complex flow characteristics. Including Ke et al. [18] and some other  
5 researchers [17], these studies emphasize the crucial role of these factors in reducing  
6 the likelihood of keyhole collapse, suppressing bubble formation, facilitating easy gas  
7 escape, and significantly reducing the quantity and size of voids. Furthermore, Fetzer  
8 et al. and Tao & Yang [19, 20] observed that during the LCOW process, bubbles initially  
9 form at the turning points of the laser beam path, subsequently interacting with the  
10 oscillating laser beam during the welding process. This interaction assists in eliminating  
11 bubbles during the second oscillation cycle, greatly decreasing the occurrence of gaps  
12 and promoting more consistent welding outcomes. In the research of many scholars [15,  
13 21-24], similar mechanisms have been mentioned: LCOW generates a broader molten  
14 pool, leading to lower temperature gradients during processing. Consequently, more  
15 turbulence is induced, disrupting the growth of columnar crystals and promoting the  
16 formation of equiaxed crystals. These grain characteristics effectively reduce the  
17 occurrence of cracks, further enhancing overall welding quality. LCOW is an advanced  
18 welding technique that precisely controls the shape and position of the molten pool,  
19 reducing defects and ensuring uniform heat distribution to improve welding stability  
20 [15]. High scanning frequencies can form stable keyholes and molten pools, facilitating  
21 gas escape and reducing cracks and pores [25]. Nevertheless, LCOW still requires  
22 careful parameter selection to ensure high-quality welding

23 The significance of this research lies in addressing the challenges associated with  
24 welding aluminum alloys using 3D Laser Foil Printing (LFP) and Laser Circular  
25 Oscillation Welding (LCOW). While LCOW effectively reduces welding defects,  
26 careful selection of appropriate welding parameters remains crucial to ensuring

1 consistently high-quality welding for a 3D LFP process with AA6061 foil thickness of  
2 0.3mm. To address this challenge, our approach is based on a methodology similar to  
3 the study by Tran & Lo [26], incorporating circular packing design methods with  
4 artificial neural networks using simulation results from the Flow3D software. By  
5 optimizing welding parameters through a combination of simulation models and  
6 experiments, the study aims to reduce defects such as hot cracks and improve welding  
7 quality. Additionally, a deep understanding of the processing mechanisms is pursued,  
8 demonstrating how appropriate laser energy density and scanning speed can effectively  
9 control the shape and size of the molten pool, thus influencing weld quality. These  
10 techniques aim to create comprehensive processing charts that help determine the most  
11 suitable welding parameters to eliminate welding defects consistently. Ultimately, these  
12 processing maps will serve as invaluable guides for selecting appropriate parameters  
13 for different welding criteria, comprehensively enhancing the overall quality of laser  
14 welding in the 3D LFP process.

## 15 **2. Methodologies**

16 To generate a processing map, a sufficient number of simulation data sets are  
17 required to accurately predict the optimal processing parameters. The initial step  
18 involves conducting simultaneous simulations and experiments to determine whether  
19 the error in the results under the same processing conditions is acceptable. Once the  
20 accuracy of the model has been confirmed, a large number of simulations are carried  
21 out by using a circle packaging design method. Data obtained from these simulations  
22 are then used in artificial neural network algorithms to generate processing maps. This  
23 map displays the optimal processing parameters for achieving high-quality welds by  
24 plotting different processing maps based upon different criteria such as weld  
25 penetration depth, weld interface width between foil and substrate, and laser scanning

1 frequency to evaluate the quality of the resulting welds. As a result, it enables the  
2 identification of the optimal processing parameters for specific welding criteria for a  
3 3D LFP process.

4 These optimal parameters in the processing map are then utilized for the  
5 subsequent process of 3D LFP for demonstration. Through a series of carefully  
6 conducted experiments and thorough post-processing procedures, the primary objective  
7 of this observation is to assess and ascertain whether these features demonstrate  
8 commendable mechanical properties.

## 9 **2.1 Experimental setup**

10 During the experiment, AA6061 foil with a thickness of 0.3mm was bonded with  
11 AA6061 substrate with a thickness of 5 mm in a 3D LFP process. The laser welding  
12 system includes a continuous-wave (CW) fiber laser (YLR-1000-MM-WC, IPG  
13 Photonics, U.S.A.) that operates at a wavelength of 1070 nm, a maximum power of  
14 1000 W, M2 of 3.52, a collimated beam waist diameter of 9.6 mm (a 50  $\mu\text{m}$  beam was  
15 out of fiber and expanded through a collimator with a focal length of 100 mm), and a  
16 spot size of 127  $\mu\text{m}$  [27], as well as a galvo-mirror scanner (HurrySCAN20, SCANLAB,  
17 Germany) and a F- $\theta$  lens (focal length: 254 mm, THORLABS, U.S.A.). Initially, spot  
18 welding was utilized as the method of affixing the upper foil to the lower substrate. This  
19 initial step provided a stable connection between the two foils, and then the subsequent  
20 phases of experimentation followed, involving the application of varying laser welding  
21 parameters.

22 Aluminum oxidation is also an issue, as the naturally forming aluminum oxide  
23 ( $\text{Al}_2\text{O}_3$ ) layer affects the welding process. While it slightly reduces reflectivity by  
24 absorbing some laser energy, it also acts as a thermal barrier, hindering heat transfer  
25 and causing uneven heating. The oxide layer can introduce contamination into the weld

1 pool, leading to inclusions and weakening the weld. To mitigate these issues, before  
2 each experiment, we clean the aluminum foil surface with alcohol to minimize the  
3 impact of the oxide layer on the welding process. Additionally, employing techniques  
4 like beam oscillation can further enhance welding quality by stabilizing the keyhole.

5 The trajectory of the heat source, alongside its pertinent characteristics in LCOW,  
6 is depicted in Fig. 1. The heat source rotates along a circular path, which is characterized  
7 by the swing width represented by "A". The A value used later for simulation and  
8 experiment is fixed at 0.7mm, and the tangential velocity is represented by " $V_t$ ".  
9 Simultaneously, the center of this circular path maintains a consistent forward  
10 movement along the welding direction at a steady speed termed " $V_f$ ". This orchestrated  
11 motion ensures a predefined degree of overlap with each revolution. The parameter  
12 controlling the number of oscillations executed by the heat source within specific time  
13 intervals is referred to as the scanning frequency, represented as " $f$ ". At the same time,  
14 "Overlap" represents the percentage of overlap area between laser scanning paths along  
15 each circular path, and the value used for simulations and experiments will be fixed at  
16 80%. To simplify the simulation and experimental processes and to optimize  
17 performance, we fixed the parameters "A", "f", and "overlap" based on preliminary  
18 experimental results. This approach reduced the complexity of the simulation by  
19 limiting the number of varying parameters. The chosen values for amplitude (0.7mm),  
20 frequency, and overlap (80%) provided the best results, minimizing defects such as  
21 cracks and pores while ensuring high-quality welds.

22 The integrated movement pattern that governs the heat source can be  
23 mathematically formulated using Eq. (1). The values of " $f$ " and " $V_f$ " can be expressed  
24 using Eqs. (2) and (3), respectively [28].

25 According to Kang et al. [12] study, it is mentioned that when the scanning  
26 frequency exceeds 150Hz, the sensitivity to cracks significantly decreases. Therefore,

1 the experimental parameter selection for validating simulation results in this study will  
2 reference this value. The range covers frequencies greater than, less than, and equal to  
3 150Hz, aiming to examine whether the experimental results can observe this clear trend.  
4 The specific parameters employed in this experimental endeavor are meticulously  
5 documented in Table 1.

$$\begin{cases} x(t) = \frac{A}{2} \cos\left(\frac{2V_t}{A}t\right) + V_f t \\ y(t) = \frac{A}{2} \sin\left(\frac{2V_t}{A}t\right) \end{cases} \quad (1)$$

$$f = \frac{V_t}{\pi A} \quad (2)$$

$$V_f = f \left( A - \left( \frac{A \cdot \text{Overlap}}{100} \right) \right) \quad (3)$$

6

## 7 2.2 Simulation setup

8 The commercial simulation software FLOW-3D is used for the LCOW simulation  
9 in this study. During the simulation process, to improve computational efficiency while  
10 maintaining simulation accuracy, an appropriate model size and performed mesh  
11 segmentation are needed. In this model, a suitable size is selected to ensure that the  
12 simulation can be completed in a reasonable time and with sufficient accuracy.  
13 Specifically, the model is divided into many small meshes to better control the  
14 computational load and accuracy. The model size and mesh segmentation are shown in  
15 Fig. 2.

16 The following content explains the relevant assumptions and control equations  
17 used in the development of the CFD model. Assuming that the energy density of the  
18 laser beam presents a Gaussian distribution, and its profile has the characteristics of a  
19 Gaussian-like axially symmetric distribution type. Therefore, the heat source modeling  
20 of the CFD model can be expressed as [29]:

$$q = Q \cdot \exp \left[ - \left( \frac{r}{r_b} \right)^2 \right] \quad (4)$$

1 where  $q$  is the heat density function,  $Q$  is the heat density value at the center of the beam,  
 2  $r$  is the radial coordinate, and  $r_b$  is the laser spot radius at the focal plane. The ray path  
 3 modeling of laser emission is based on ray tracing technology based on the real-time  
 4 multi-reflection model in Flow3D®. At the same time, the movement of the keyhole-  
 5 free surface during the welding process is tracked using the volume of fluid method  
 6 (VOF).

7 The mass conservation equation is expressed as [30]:

$$\nabla \cdot v = \frac{\dot{m}_s}{\rho} \quad (5)$$

8 where  $\rho$  is the fluid density,  $v$  is the velocity vector, and  $\dot{m}_s$  is the mass source term  
 9 contributed by the metal droplet. The energy conservation equation is expressed as  
 10 [30]:

$$\frac{\partial h}{\partial t} + v \cdot \nabla h = \frac{1}{\rho} \nabla \cdot (k \nabla T) \quad (6)$$

11 where  $h$  is the enthalpy and  $T$  is the temperature. However, body forces are ignored in  
 12 the equation. In this simulation modeling, the solid-liquid phase transition is described  
 13 using an entropy-based continuum model, such as [30]:

$$h = \begin{cases} \rho_s C_s T & (T \leq T_s) \\ h(T_s) + h_{sl} \frac{T - T_s}{T_l - T_s} & (T_s \leq T \leq T_l) \\ h(T_l) + \rho_l C_l (T - T_l) & (T_l \leq T) \end{cases} \quad (7)$$

14 where  $\rho_s$  and  $\rho_l$  are the solid and liquid densities,  $C_s$  and  $C_l$  are the specific heats per  
 15 unit volume of the solid and liquid phases,  $T_s$  and  $T_l$  are the solidus and liquidus  
 16 temperatures, and  $h_{sl}$  is the melting Latent heat. It is noted that the fluid volume  
 17 equation used to track the movement of the free surface of the keyhole is expressed as  
 18 [30]:

$$\frac{\partial F}{\partial t} + \nabla \cdot (vF) = \dot{F}_s \quad (8)$$

1 where  $F$  is the volume of fluid,  $v$  is the velocity vector, and  $\dot{F}_s$  is the change of the  
 2 volume fraction of fluid associated with the mass source term  $\dot{m}_s$  in the mass continuity  
 3 equation. The keyhole is mainly controlled by the recoil pressure generated by the  
 4 evaporation of the molten metal in the weld pool. In addition, the recoil pressure,  $P_R$ ,  
 5 acting on the keyhole wall can be expressed by the following formula [30]:

$$P_R(T) \cong 0.54P_{sat}(T) \cong 0.54P_0 \exp L_v \frac{T - T_b}{RTT_b} \quad (9)$$

6 where  $P_{sat}$  is the saturation pressure,  $P_0$  is the atmospheric pressure, and  $L_v$  is the latent  
 7 heat of vaporization,  $T_b$  is the boiling temperature, and  $R$  is the universal gas constant.

8 Next, the boundary conditions used in this simulation modeling are explained. The  
 9 top and bottom surfaces of the calculation domain are specified with outflow conditions.  
 10 They are assumed to be subject to heat conduction, heat convection, heat radiation, and  
 11 evaporation effects, which can be expressed by Eq. (10). And the four sides of the model  
 12 are designated as continuous conditions. They can be expressed by the following Eq.  
 13 (11) [31].

$$\begin{cases} k \frac{\partial T}{\partial \vec{n}} = -h_c(T - T_0) - \varepsilon_r \sigma(T^4 - T_0^4) - \rho V_{evap} T & (10) \\ k \frac{\partial T}{\partial \vec{n}} = -h_c(T - T_0) - \varepsilon_r \sigma(T^4 - T_0^4) & (11) \end{cases}$$

14 where  $\vec{n}$  is the normal vector to the surface,  $h_c$  is the convection coefficient,  $T_0$  is the  
 15 ambient temperature,  $\varepsilon_r$  is the radiation coefficient,  $\sigma$  is the Stefan-Boltzmann constant,  
 16 and  $V_{evap}$  is the free surface decay due to evaporation speed. The physical  
 17 characteristics of the materials, such as thermal conductivity, specific heat, and density,  
 18 were considered to vary as a function of temperature  $T$  (K). This approach differs from  
 19 previous studies [32], where these properties were often assumed to be constant.

20 It is noted that simulations are conducted using the Intel(R) Xeon(R) E5-2630 v4  
 21 10-core processor (CPU). The average time required for each simulation mainly

1 depends on the scanning speed. Simulations carried out at lower scanning speeds take  
2 an average of approximately 7 - 8 hours, while those at higher scanning speeds take an  
3 average of approximately 3 - 4 hours.

### 4 **3. Results of Experimental and Simulation Data**

#### 5 **3.1 Experimental results**

6 In the meticulous experimental process, three sets of different processing  
7 parameters were deliberately employed, including a low scanning frequency and a high  
8 scanning frequency. This approach allows for careful observation and evaluation of the  
9 experimental results under various processing conditions. The difference in scanning  
10 frequency primarily depends on the speed at which the laser scans the aluminum alloy  
11 material during the welding process. To enhance the stability of LCOW technology,  
12 point welding practices were further employed to securely fix the aluminum alloy  
13 material in place. This strategic step enables better control of the welding process,  
14 thereby enhancing the overall stability of the material during welding.

15 The experimental results observed using an optical microscope, as depicted in Fig.  
16 3, particularly emphasize the remarkable effectiveness of employing high scanning  
17 frequency processing parameters to mitigate the sensitivity to crack formation during  
18 the welding process. A meticulous examination of Fig. 3 brings forth a series of  
19 compelling insights. For instance, upon scrutiny of the upper surface of the weld  
20 executed under the parameter set of 600 W - 300 mm/s at the frequency of 136 Hz,  
21 distinct patterns of elongated cracks become evident. This behavior may be attributed  
22 to the inadequate scanning frequency employed in this specific instance. The utilization  
23 of a lower scanning frequency failed to elicit a satisfactory quantity of equiaxed grains  
24 within the weld structure. Consequently, the resultant cracks propagated along the  
25 boundaries of the columnar grains, exacerbating the underlying issue.

1 In marked contrast, a profoundly different outcome emerged when inspecting the  
2 upper surfaces of welds conducted under parameter sets of 700 W – 350 mm/s at the  
3 frequency of 159 Hz and 800 W – 400 mm/s at the frequency of 182 Hz. Notably absent  
4 were any discernible large-scale cracks, underscoring the judicious application of high  
5 scanning frequency. This deliberate selection facilitated the development of a  
6 substantial proportion of equiaxed grains within the weld structure, consequently  
7 significantly curbing the propensity for crack propagation along grain boundaries. In  
8 this context, the intricate nature of the grain boundaries played a pivotal role in  
9 impeding the facile advancement of cracks. The temperature gradient data derived from  
10 the simulation results, as shown in the Fig. 4, also indicates that the temperature  
11 gradient under the processing parameters of 600W – 300mm/s is much higher than that  
12 of the other two sets of processing parameters with higher scanning frequencies. This  
13 does not provide a suitable processing environment for the growth of equiaxed grains  
14 during the process. The implications of these findings are substantial, especially  
15 considering the prevalent challenges linked to crack formation within the realm of  
16 aluminum alloy welding.

### 17 **3.2 Comparison error between simulation and experimental results**

18 The comparison between the simulation and experimental results is presented in  
19 Fig. 5. It can be seen that the model used in this simulation has a certain level of  
20 similarity in predicting the weld geometry. It is found that the errors of width and depth  
21 of the weld bead in Fig. 6 and Fig. 7 were within approximately 10%. In this study,  
22 experiments were conducted three times with different parameters. The measurements  
23 of the weld bead dimensions in the experimental samples compared with the  
24 simulations represent the average values from these three experiments. This finding  
25 indicates that the model possesses sufficient accuracy to conduct extensive simulations

1 using different processing parameters. Such a high level of accuracy enables us to  
2 confidently employ the model to forecast the outcome of the welding process under  
3 varying conditions and optimize the process parameters to attain the desired outcomes.  
4 Accurately predicting the welding outcome under different conditions is crucial in  
5 developing efficient and effective welding processes. Through the use of this simulation  
6 model, it is possible to streamline the process and avoid undertaking a significant  
7 number of trial-and-error experiments. Instead, simulations can be employed to  
8 ascertain the optimal parameters for achieving the desired results.

### 9 **3.3 Establish the circular packaging design model after confirming the accuracy** 10 **of the model**

11 In this study, an Artificial Neural Network (ANN) model was developed to predict  
12 melt pool dimensions and peak temperatures based on finite element (FE) simulations.  
13 The ANN was trained using a dataset of 36 FE simulation results, with the data points  
14 selected via a circle packing design algorithm optimized with a radius of 0.075. This  
15 design ensured a uniform distribution of sampling points across the design space while  
16 balancing prediction accuracy and computational cost. The model was implemented  
17 using backpropagation with a single hidden layer consisting of ten nodes. The  
18 performance of the ANN was evaluated using the relative mean squared error (RMSE)  
19 metric, demonstrating reliable prediction capabilities for the given application.

20 After verifying the reliability and accuracy of the model, the initial large-scale  
21 simulation input design phase using circular packaging design methods begins [33].  
22 However, it's important to note that these simulations are based on an extremely limited  
23 set of input conditions. This limitation raises concerns about our ability to accurately  
24 predict permutations within the extensive range of different parameters within the  
25 design space. This limitation primarily arises from the fact that these comprehensive  
26 simulations may not necessarily include the critical optimization parameters needed to

1 enhance the quality of laser-welded lap joints.

2 In summary, it is essential to consider alternative methods, such as artificial neural  
3 networks, to address this constraint and ensure a thorough exploration of the entire  
4 design space. These neural networks will serve as an alternative modeling approach,  
5 enabling us to predict the corresponding weld seam depth, width, and scanning  
6 frequency based on given inputs such as laser power and tangential scanning speed.  
7 This approach allows us to traverse the entire design space and generate processing  
8 maps with high predictive capabilities. It is noted that Fig. 8 provides an intuitive  
9 illustration of the process for generating these processing maps [26].

10 In this study, one potential application is to use ANNs to generate processing maps  
11 for the depth, width, and frequency of the weld bead, respectively. There are a total of  
12 36 sets of processing parameters for using the circular packaging design method to  
13 generate processing maps, covering a wide range from low power and low welding  
14 speed to high power and high welding speed. This was done to ensure that there were  
15 enough simulation data points to generate an accurate processing map that covers the  
16 entire range of processing conditions.

17 In Fig. 9, once the ANN model is trained and validated, it can be used to generate  
18 processing maps that show the predicted depth, width, and frequency of the weld bead  
19 for different combinations of welding parameters. These maps can be useful for  
20 optimizing the welding process and achieving desired weld characteristics for a 3D LFP  
21 process. The accuracy of the ANN model during the entire training, validation, and  
22 testing process is depicted in Fig. 10. Ultimately, the overall R value of the ANN model  
23 for forecasting the target value stood at 0.99, demonstrating an average precision of  
24 99% across its predictions during training, validation, and testing.

### 25 **3.4 Criteria of weld bead depth, width, and frequency processing maps**

1 After using the ANN module in MATLAB to generate the processing maps of weld  
2 depth, width, and frequency to finally obtain the optimized parameters without any  
3 defects such as pores and cracks in the weld, first, the threshold settings in these maps  
4 respectively are very important. Therefore, the criteria for bead depth, width, and  
5 frequency are respectively described below.

6 ● Criteria of weld bead depth:

7 As depicted in Fig. 11, an interesting observation arises from the results of  
8 the FLOW-3D simulation. When the keyhole exhibits a noticeably higher depth-  
9 to-width ratio, a collapse of the keyhole occurs, with an average weld depth of  
10 around 0.95mm in such instances. Zhang et al.'s study [17] mentions that in  
11 welding processes with unstable conditions, a higher depth-to-width ratio makes  
12 the keyhole prone to collapse, resulting in the formation of bubbles at the bottom  
13 of the weld. Additionally, at this point, the keyhole, as mentioned in Ke et al.'s  
14 study [18], exhibits stable characteristics with an enlarged opening, resulting in a  
15 shallower and wider molten pool with a lower aspect ratio. This facilitates the  
16 escape of bubbles and reduces the likelihood of keyhole collapse. This adjustment  
17 is strategically aimed at reducing the risk of keyhole collapse. Additionally, it  
18 provides ample time for the escape of any bubbles, thereby minimizing porosity  
19 within the weld. However, when the weld depth falls below 0.6mm, despite the  
20 relatively lower aspect ratio of the keyhole, it fails to achieve an adequate welding  
21 depth, thereby adversely affecting the joint's performance. In summary, the  
22 optimal parameter within the depth range of 0.6 mm to 0.95 mm is set as criteria.

23 ● Criteria of weld bead width:

24 As depicted in Fig. 12, it's apparent that as the depth increases, the energy  
25 conveyed by the laser gradually diminishes, resulting in a gradual reduction in  
26 weld width as the depth increases. However, the analysis of the FLOW-3D

1 simulation results has revealed a significant trend. In such a scenario, it exhibits  
2 characteristics similar to insufficient penetration in welding, as discussed in  
3 Dimatteo et al.'s study [28], where inadequate laser penetration energy leads to  
4 insufficient welding. It is worth noting that the simulation results confirm that for  
5 a sufficient melt depth, which is a weld penetration depth ranging from 0.60 to  
6 0.95 mm, the average interface width between the foil and substrate is  
7 approximately 1.05 mm. Hence, the optimized parameter was determined as the  
8 condition where the width of the weld seam at the interface between the foil and  
9 substrate exceeds 1.05 mm as criteria.

10 ● Criteria of scanning frequency:

11 In the research findings by Kang et al. [12], it is noted that as the scanning  
12 frequency of LCOW reaches 100 Hz and beyond, the thermal crack susceptibility  
13 in 6xxxx series aluminum alloys decreases progressively with the increasing width.  
14 Following a series of experiments, as depicted in Fig. 13, it has been established  
15 that an approximate scanning frequency of 150 Hz effectively reduces the  
16 formation of cracks. Notably, the scanning frequency in this study is contingent  
17 upon the tangential speed of the laser during the processing. Therefore, the  
18 optimized parameter was determined wherein the scanning frequency exceeded  
19 150 Hz with a corresponding tangential speed value of approximately 330 mm/s  
20 as criteria.

21 Finally, after overlaying and merging the processing maps defined by the  
22 optimized parameter as criteria for weld depth, width, and scanning frequency, finally,  
23 a processing map with different weld characteristics in different internal regions can be  
24 obtained, as shown in Fig. 14. The relevant discussion of the different weld properties  
25 in each region will be explained in next subsection.

### 1    **3.5 Feasibility of the optimized processing map**

2            Subsequently, selecting 7 specific machining parameters from the processing map  
3    for conducting experiments is proceeded. The objective was to validate whether the  
4    experimental results aligned with the optimized parameters predicted by simulation and  
5    ANN models. In Fig. 15, the experimental results were displayed in longitudinal cross-  
6    sections of welds within different region ranges. In addition, Fig. 16 shows the  
7    experimental outcomes of the upper surfaces of welds in various region ranges.  
8    Through careful observation in Fig. 15 and Fig. 16, it is possible to deduce various  
9    patterns:

10    ●    Green Region:

11            In that particular region, the experimental results using optimally balanced  
12    parameters for weld depth, width, and frequency have shown welds free from any  
13    pores or cracks.

14

Accepted Manuscript Not Certified

1 ● Black Region:

2 In this region, although the experimental outcomes showed no porosity,  
3 cracks formed in Fig. 15 and Fig. 16 due to insufficient frequency. It is worth  
4 noting that during the sample grinding process, the grinding is done to the center  
5 line of the weld. However, the cracks observed on the upper surface appear to  
6 originate from a position slightly to the right of the weld. Therefore, cracks cannot  
7 be observed on the longitudinal cross-section of the sample.

8 ● Blue Region:

9 While the experimental outcomes within the blue region did not produce  
10 cracks on the weld surface due to the utilization of a suitably high welding speed  
11 and an elevated frequency, they fell short in creating welds with the requisite depth  
12 owing to the lower laser power. It is worth noting that due to the tendency of  
13 aluminum foil to deform. At the same time, thermal stress occurs during  
14 processing, even though spot welding has been applied before a LFP process, it  
15 remains challenging to maintain full contact with each other. Therefore, in the  
16 weld results of the blue region, gaps in Fig. 15 can be observed forming between  
17 the foil and the substrate.

18 ● Red region:

19 Experimental results within this region indicated a higher incidence of  
20 porosity. Notably, in these experiments, employing a welding speed of 200 mm/s  
21 led to crack formation, as illustrated in Fig. 16, due to inadequate frequency.

22 From the above experimental outcomes in Fig. 15 and Fig. 16, it is evident that the  
23 optimal processing map generated by the simulation and ANN models closely matched  
24 the experimental results, showcasing a high level of reliability.

25

### 1 **3.6 Characterization of pores and cracks in 3D LFP parts and comparison of** 2 **surface roughness differences**

3 After determining the optimized parameter ranges from Section 4, one parameter  
4 set in the green region is selected to manufacture LFP samples, and one optimal  
5 parameter set based upon a non-oscillating laser welding (NOLW) strategy [34] to  
6 manufacture LFP samples to compare experimental results. Table 2 shows the  
7 optimized processing parameters of experimental samples using two different scanning  
8 strategies, and all the number of stacking layers for each sample is 5.

9 Next, a comparative analysis of the experimental samples using different scanning  
10 strategies was conducted. Using a scanning electron microscope (SEM) to observe the  
11 upper surfaces of the two samples, as shown in Fig. 17 and Fig. 18 cracks were observed  
12 on the upper surface of the sample using the NOLW strategy. However, no significant  
13 cracks were observed on the upper surface of the experimental sample using the LCOW  
14 strategy. This difference may be attributed to the use of laser beam oscillation, which  
15 can create favorable low-temperature gradient processing conditions for the growth of  
16 equiaxed grains. A sufficient proportion of equiaxed grains is generated in the weld  
17 seam to prevent cracks from extending along the columnar grain boundaries. However,  
18 interesting differences in results in Fig. 19 and Fig. 20 were observed in the cross-  
19 sections of the two experimental samples. It was found that numerous pores of varying  
20 sizes were observed on the cross-section of the sample with the NOLW strategy. The  
21 calculated porosity rate for this cube sample was 0.41%. In contrast, for the  
22 experimental sample with the LCOW strategy, only sporadic and extremely small pores  
23 were observed on its cross-section, with a calculated porosity of only 0.12% in a cube  
24 sample.

25 The reason for this difference may be attributed to the use of the LCOW strategy,

1 which ensures continuous stirring of the molten pool throughout the process.  
2 Additionally, it avoids excessively concentrated heat input, preventing the keyhole  
3 depth-to-width ratio from becoming too large and susceptible to collapse. These various  
4 characteristics contribute to a lower probability of pore formation as compared to the  
5 NOLW strategy.

6 Then, a white light interferometer (Model: Bruker Contour GT-K) was used to  
7 measure the surface roughness, and the surface morphology characteristics of the two  
8 samples by the NOLW and LCOW strategies were discussed and compared. As shown  
9 in Fig. 21 and Fig. 22, the black area in the figure is due to the large height difference  
10 on the sample surface, which causes the light to be incident and unable to be  
11 successfully reflected back to the instrument, resulting in the loss of measurement data.  
12 It can be seen that the measurement results of NOLW have more differences as  
13 compared to those of LCOW. There are many black areas, which means that the surface  
14 of the NOLW sample is not smoother than that of the LCOW sample. There are more  
15 measurement points with excessive height differences on the surface. The surface  
16 roughness of the sample using LCOW is much lower than that of the NOLW sample. It  
17 is found that the average  $S_a$  value is only  $7.27\mu\text{m}$  for the LCOW sample, while the  
18 average  $S_a$  value is  $20.87\mu\text{m}$  for the NOLW one.

19 The reason for the difference may be that the circular rotation motion trajectory of  
20 scanning avoids excessive concentration of energy, disperses the heat input, and has  
21 more stable molten pool characteristics, thereby reducing the generation of spatter,  
22 making the sample have a relatively smooth surface.

#### 23 **4. Conclusions and suggestions**

24 This study has presented a method based on computational fluid dynamics (CFD)  
25 simulations using Flow3D and a surrogate modeling approach for determining the  
26 optimal processing parameters for 3D Laser Foil Printing (LFP) in the fabrication of

1 Laser Circular Oscillation Welding (LCOW) technique with a wobble strategy. The  
2 major contributions and findings of the present study can be summarized as follows:

- 3 ➤ The CFD simulation results demonstrated a high degree of accuracy when  
4 compared to experimental data, with a discrepancy of approximately 10%,  
5 confirming the reliability of the simulation model.
- 6 ➤ By employing an iterative process of experimentation and simulation, and  
7 incorporating machine learning for generating processing diagrams, the study  
8 successfully identified the optimal LCOW parameters for the 3D LFP process.
- 9 ➤ The optimized parameters effectively removed common welding defects,  
10 including pores and cracks, typically observed in aluminum alloy welds.
- 11 ➤ Samples processed using the optimized parameters (800 W, 550 mm/s, and 227  
12 Hz) displayed no typical aluminum alloy welding defects on the upper surface.  
13 The surface roughness was significantly reduced to 7.27  $\mu\text{m}$ , and porosity was  
14 minimized to 0.12%.

15 The optimized parameters can be furthermore defined to consistently create high-  
16 quality welds by additionally including the simulation results in modeling the  
17 microstructure in future work. It's important to note that this optimization process is not  
18 a one-time effort but an ongoing one. With the development of new materials, welding  
19 processes, and technologies, the optimal parameters for LCOW may need to be  
20 reassessed and updated. Through systematic and rigorous experimentation, simulation,  
21 and optimization, it is possible to continually enhance the quality of LCOW in the 3D  
22 LFP process.

## 23 **Acknowledgments**

24 The support for this research was provided by the Division of Engineering and  
25 Technology Research and Development of the National Science and Technology  
26 Council under Grant No. MOST 111-2223-E-006-002 is appreciated.

## 27 **References**

- 28 [1] C.-H. Hung, T. Turk, M. H. Sehhat, and M. C. Leu, "Development and  
29 experimental study of an automated laser-foil-printing additive manufacturing  
30 system," *Rapid Prototyping Journal*, vol. 28, no. 6, pp. 1013-1022, 2022.
- 31 [2] C.-H. Hung, W.-T. Chen, M. H. Sehhat, and M. C. Leu, "The effect of laser welding  
32 modes on mechanical properties and microstructure of 304L stainless steel

- 1 parts fabricated by laser-foil-printing additive manufacturing," *The*  
2 *International Journal of Advanced Manufacturing Technology*, vol. 112, pp.  
3 867-877, 2021.
- 4 [3] C. Chen, Y. Shen, and H.-L. Tsai, "A foil-based additive manufacturing  
5 technology for metal parts," *Journal of Manufacturing Science and Engineering*,  
6 vol. 139, no. 2, p. 024501, 2017.
- 7 [4] C.-H. Hung, Y. Shen, M.-C. Leu, and H.-L. Tsai, "Mechanical Properties of 304L  
8 Parts Made by Laser-Foil-Printing Technology," 2017.
- 9 [5] C.-H. Hung, A. Sutton, Y. Li, Y. Shen, H.-L. Tsai, and M. C. Leu, "Enhanced  
10 mechanical properties for 304L stainless steel parts fabricated by laser-foil-  
11 printing additive manufacturing," *Journal of Manufacturing Processes*, vol. 45,  
12 pp. 438-446, 2019/09/01/ 2019, doi:  
13 <https://doi.org/10.1016/j.jmapro.2019.07.030>.
- 14 [6] C.-H. Hung *et al.*, "Aluminum parts fabricated by laser-foil-printing additive  
15 manufacturing: processing, microstructure, and mechanical properties,"  
16 *Materials*, vol. 13, no. 2, p. 414, 2020.
- 17 [7] Y. Kawahito, N. Matsumoto, Y. Abe, and S. Katayama, "Laser absorption of  
18 aluminium alloy in high brightness and high power fibre laser welding,"  
19 *Welding International*, vol. 26, no. 4, pp. 275-281, 2012.
- 20 [8] M. Sheikhi, F. M. Ghaini, and H. Assadi, "Prediction of solidification cracking in  
21 pulsed laser welding of 2024 aluminum alloy," *Acta Materialia*, vol. 82, pp. 491-  
22 502, 2015.
- 23 [9] J. F. Ready, *Industrial applications of lasers*. Elsevier, 1997.
- 24 [10] H.-Y. Wang, Y.-L. Lo, H.-C. Tran, M. M. Raza, and T.-N. Le, "Systematic approach  
25 for reducing micro-crack formation in Inconel 713LC components fabricated by  
26 laser powder bed fusion," *Rapid Prototyping Journal*, vol. 27, no. 8, pp. 1548-  
27 1561, 2021.
- 28 [11] H.-H. Chen, Y.-L. Lo, Y.-Y. Hsu, and K.-L. Lai, "Systematic optimization of L-PBF  
29 processing parameters for Al alloy 6061 with YSZ nanoparticles," *Optics & Laser*  
30 *Technology*, vol. 167, p. 109676, 2023/12/01/ 2023, doi:  
31 <https://doi.org/10.1016/j.optlastec.2023.109676>.
- 32 [12] M. Kang, J. Cheon, D. H. Kam, and C. Kim, "The hot cracking susceptibility  
33 subjected the laser beam oscillation welding on 6XXX aluminum alloy with a  
34 partial penetration joint," *Journal of Laser Applications*, vol. 33, no. 1, 2020, doi:  
35 10.2351/7.0000319.
- 36 [13] J. Han, Y. Shi, J.-c. Guo, K. Volodymyr, W.-y. Le, and F.-x. Dai, "Porosity inhibition  
37 of aluminum alloy by power-modulated laser welding and mechanism  
38 analysis," *Journal of Manufacturing Processes*, vol. 102, pp. 827-838, 2023.

- 1 [14] V. V. Pamarthi, T. Sun, A. Das, and P. Franciosa, "Tailoring the weld  
2 microstructure to prevent solidification cracking in remote laser welding of  
3 AA6005 aluminium alloys using adjustable ringmode beam," *Journal of*  
4 *Materials Research and Technology*, vol. 25, pp. 7154-7168, 2023.
- 5 [15] L. Wang, M. Gao, C. Zhang, and X. Zeng, "Effect of beam oscillating pattern on  
6 weld characterization of laser welding of AA6061-T6 aluminum alloy,"  
7 *Materials & Design*, vol. 108, pp. 707-717, 2016.
- 8 [16] L. Cen, W. Du, M. Gong, Y. Lu, C. Zhang, and M. Gao, "Effect of high-frequency  
9 beam oscillation on microstructures and cracks in laser cladding of Al-Cu-Mg  
10 alloys," *Surface and Coatings Technology*, vol. 447, p. 128852, 2022.
- 11 [17] C. Zhang, Y. Yu, C. Chen, X. Zeng, and M. Gao, "Suppressing porosity of a laser  
12 keyhole welded Al-6Mg alloy via beam oscillation," *Journal of Materials*  
13 *Processing Technology*, vol. 278, p. 116382, 2020.
- 14 [18] W. Ke, X. Bu, J. Oliveira, W. Xu, Z. Wang, and Z. Zeng, "Modeling and numerical  
15 study of keyhole-induced porosity formation in laser beam oscillating welding  
16 of 5A06 aluminum alloy," *Optics & Laser Technology*, vol. 133, p. 106540, 2021.
- 17 [19] W. Tao and S. Yang, "Weld zone porosity elimination process in remote laser  
18 welding of AA5182-O aluminum alloy lap-joints," *Journal of Materials*  
19 *Processing Technology*, vol. 286, p. 116826, 2020.
- 20 [20] F. Fetzer, M. Sommer, R. Weber, J.-P. Weberpals, and T. Graf, "Reduction of  
21 pores by means of laser beam oscillation during remote welding of AlMgSi,"  
22 *Optics and Lasers in Engineering*, vol. 108, pp. 68-77, 2018.
- 23 [21] S. Li, G. Mi, and C. Wang, "A study on laser beam oscillating welding  
24 characteristics for the 5083 aluminum alloy: Morphology, microstructure and  
25 mechanical properties," *Journal of Manufacturing Processes*, vol. 53, pp. 12-20,  
26 2020.
- 27 [22] M. Kang, H. N. Han, and C. Kim, "Microstructure and solidification crack  
28 susceptibility of Al 6014 molten alloy subjected to a spatially oscillated laser  
29 beam," *Materials*, vol. 11, no. 4, p. 648, 2018.
- 30 [23] C. Hagenlocher, M. Sommer, F. Fetzer, R. Weber, and T. Graf, "Optimization of  
31 the solidification conditions by means of beam oscillation during laser beam  
32 welding of aluminum," *Materials & Design*, vol. 160, pp. 1178-1185, 2018.
- 33 [24] H. Cheng *et al.*, "Processing modes in laser beam oscillating welding of Al6Cu  
34 alloy," *Journal of Manufacturing Processes*, vol. 68, pp. 1261-1270, 2021.
- 35 [25] M. Wu, Z. Luo, Y. Li, L. Liu, and S. Ao, "Effect of oscillation modes on weld  
36 formation and pores of laser welding in the horizontal position," *Optics & Laser*  
37 *Technology*, vol. 158, p. 108801, 2023.
- 38 [26] H.-C. Tran and Y.-L. Lo, "Systematic approach for determining optimal

- 1 processing parameters to produce parts with high density in selective laser  
2 melting process," *The International Journal of Advanced Manufacturing*  
3 *Technology*, vol. 105, pp. 4443-4460, 2019.
- 4 [27] T.-C. Huang, C.-H. Hung, and Y. Lin, "Residual stress reduction in Ti-6Al-4V parts  
5 fabricated by laser-foil-printing process," *Optics & Laser Technology*, vol. 177,  
6 p. 111157, 2024.
- 7 [28] V. Dimatteo, A. Ascari, and A. Fortunato, "Continuous laser welding with spatial  
8 beam oscillation of dissimilar thin sheet materials (Al-Cu and Cu-Al): Process  
9 optimization and characterization," *Journal of Manufacturing Processes*, vol. 44,  
10 pp. 158-165, 2019.
- 11 [29] R. Lin, H.-p. Wang, F. Lu, J. Solomon, and B. E. Carlson, "Numerical study of  
12 keyhole dynamics and keyhole-induced porosity formation in remote laser  
13 welding of Al alloys," *International Journal of Heat and Mass Transfer*, vol. 108,  
14 pp. 244-256, 2017.
- 15 [30] W.-I. Cho, S.-J. Na, C. Thomy, and F. Vollertsen, "Numerical simulation of molten  
16 pool dynamics in high power disk laser welding," *Journal of Materials*  
17 *Processing Technology*, vol. 212, no. 1, pp. 262-275, 2012.
- 18 [31] J.-H. Cho and S.-J. Na, "Implementation of real-time multiple reflection and  
19 Fresnel absorption of laser beam in keyhole," *Journal of Physics D: Applied*  
20 *Physics*, vol. 39, no. 24, p. 5372, 2006.
- 21 [32] D. Wu, X. Hua, F. Li, and L. Huang, "Understanding of spatter formation in fiber  
22 laser welding of 5083 aluminum alloy," *International Journal of Heat and Mass*  
23 *Transfer*, vol. 113, pp. 730-740, 2017.
- 24 [33] K.-T. Fang, R. Li, and A. Sudjianto, *Design and modeling for computer*  
25 *experiments*. CRC press, 2005.
- 26 [34] Y.-X. Wang, C.-H. Hung, H. Pommerenke, S.-H. Wu, and T.-Y. Liu, "Fabrication of  
27 crack-free aluminum alloy 6061 parts using laser foil printing process," *Rapid*  
28 *Prototyping Journal*, vol. 30, no. 4, pp. 722-732, 2024.
- 29  
30  
31

### 32 **List of Figure Captions:**

33  
34 Fig. 1 Schematic diagram of parameters related to LCOW path.

35 Fig. 2 Schematic diagram of the relevant dimensions of each part of the model used in  
36 this simulation.

1 Fig. 3 Photos of the upper surface of the weld bead as an experimental result observed  
2 with an optical microscope under (a) 600 W – 300 mm/s at the frequency of 136 Hz;  
3 (b) 700 W – 350 mm/s at the frequency of 159 Hz; and (c) 800 W – 400 mm/s at the  
4 frequency of 182 Hz.

5 Fig. 4 The temperature gradient data derived from the simulation results under (a) 600  
6 W – 300 mm/s at the frequency of 136 Hz; (b) 700 W – 350 mm/s at the frequency of  
7 159 Hz; and (c) 800 W – 400 mm/s at the frequency of 182 Hz.

8 Fig. 5 Comparison of experimental and simulated results for each given parameter  
9 under (a) 600 W – 300 mm/s at the frequency of 136 Hz; (b) 700 W – 350 mm/s at the  
10 frequency of 159 Hz; and (c) 800 W – 400 mm/s at the frequency of 182 Hz.

11 Fig. 6 Comparison of the width dimension between the experimental and simulation  
12 results for each given parameter

13 Fig. 7 Comparison of the depth dimension between the experimental and simulation  
14 results for each given parameter.

15 Fig. 8 Schematic diagram of the process of using the circle packaging design to apply  
16 the ANN module to generate processing maps.

17 Fig. 9 Preliminary generation of processing maps for the (a) Depth; (b) Width; and (c)  
18 Frequency of the weld bead.

19 Fig. 10 ANN model accuracy results throughout the process

20 Fig. 11 Weld bead depth in the processing map after adding the defined optimal  
21 parameter range

22 Fig. 12 Weld bead width in the processing map after adding the defined optimal  
23 parameter range.

24 Fig. 13 Weld bead frequency in the processing map after adding the defined optimal  
25 parameter range.

26 Fig. 14 Optimized depth, width, and frequency range in a processing map after

1 synthesis.

2 Fig. 15 Experimental results of the longitudinal section of weld bead with processing  
3 parameters in each area.

4 Fig. 16 Experimental results on the upper surface of the weld bead with processing  
5 parameters in each area.

6 Fig. 17 Experimental results of surface crack distribution on LFP samples using the  
7 NOLW strategy.

8 Fig. 18 Experimental results of surface crack distribution on LFP samples using the  
9 LCOW strategy.

10 Fig. 19 Experimental results of pore distribution in the cross-section of LFP samples  
11 using the NOLW strategy.

12 Fig. 20 Experimental results of pore distribution in the cross-section of LFP samples  
13 using the LCOW strategy.

14 Fig. 21 Surface roughness test results of LFP samples with the NOLW strategy.

15 Fig. 22 Surface roughness test results of LFP samples with the LCOW strategy.

16 **List of Table Headings:**

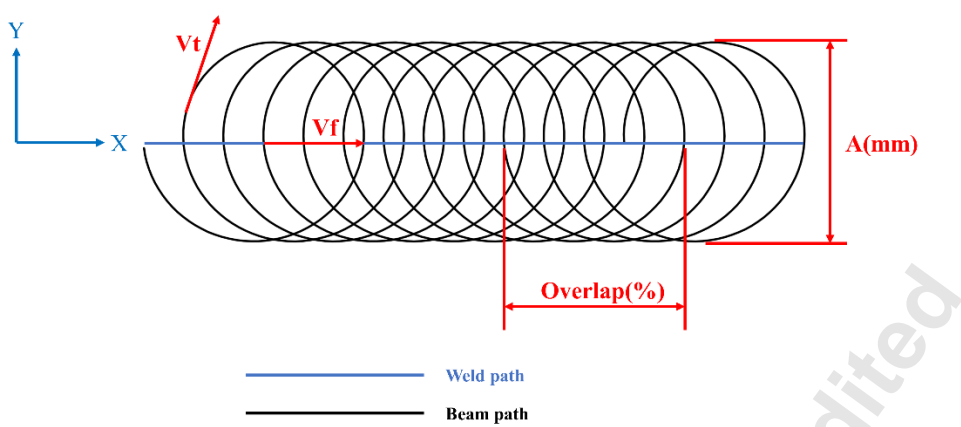
17 Table 1 Relevant parameters used in LCOW.

18 Table 2 Optimized processing parameters of experimental samples.

19

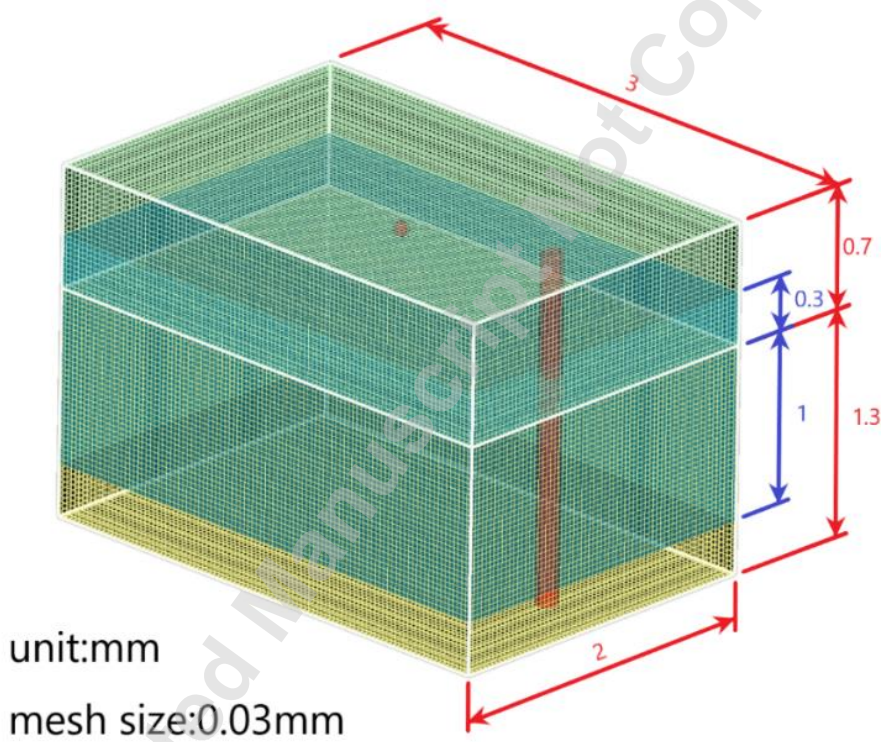
20 **Figures:**

Accepted Manuscript Not Certified



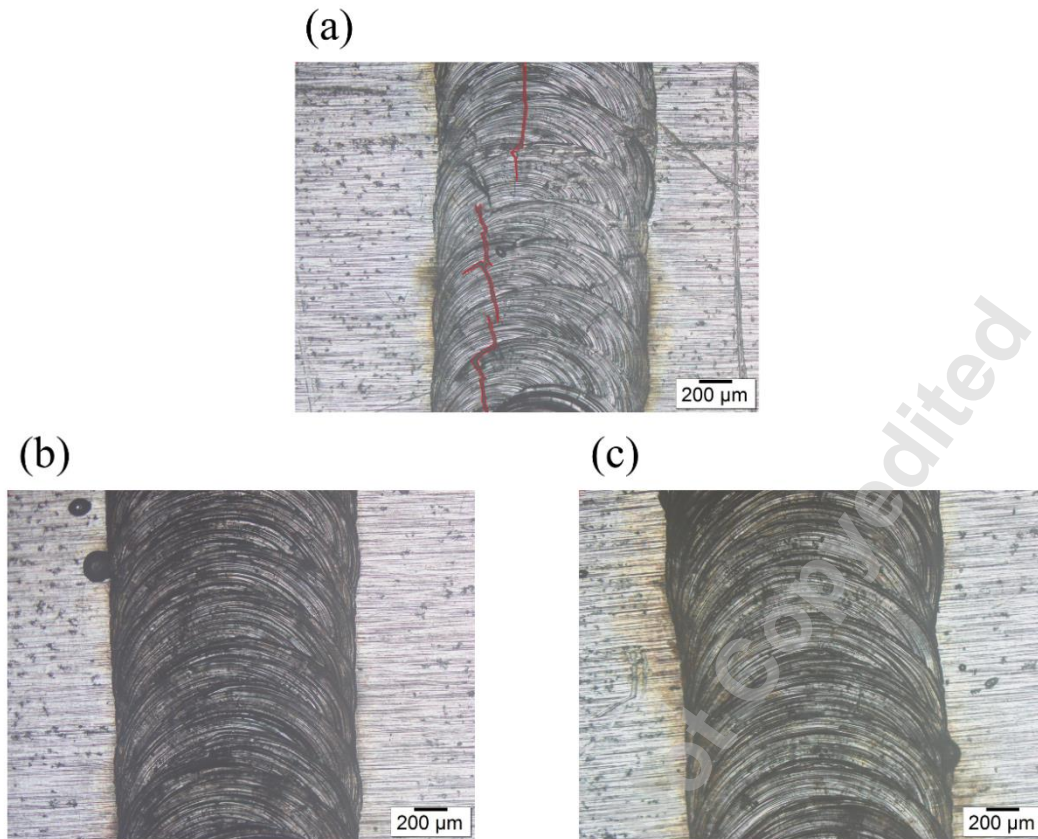
1  
2

Fig. 1 Schematic diagram of parameters related to LCOW path.



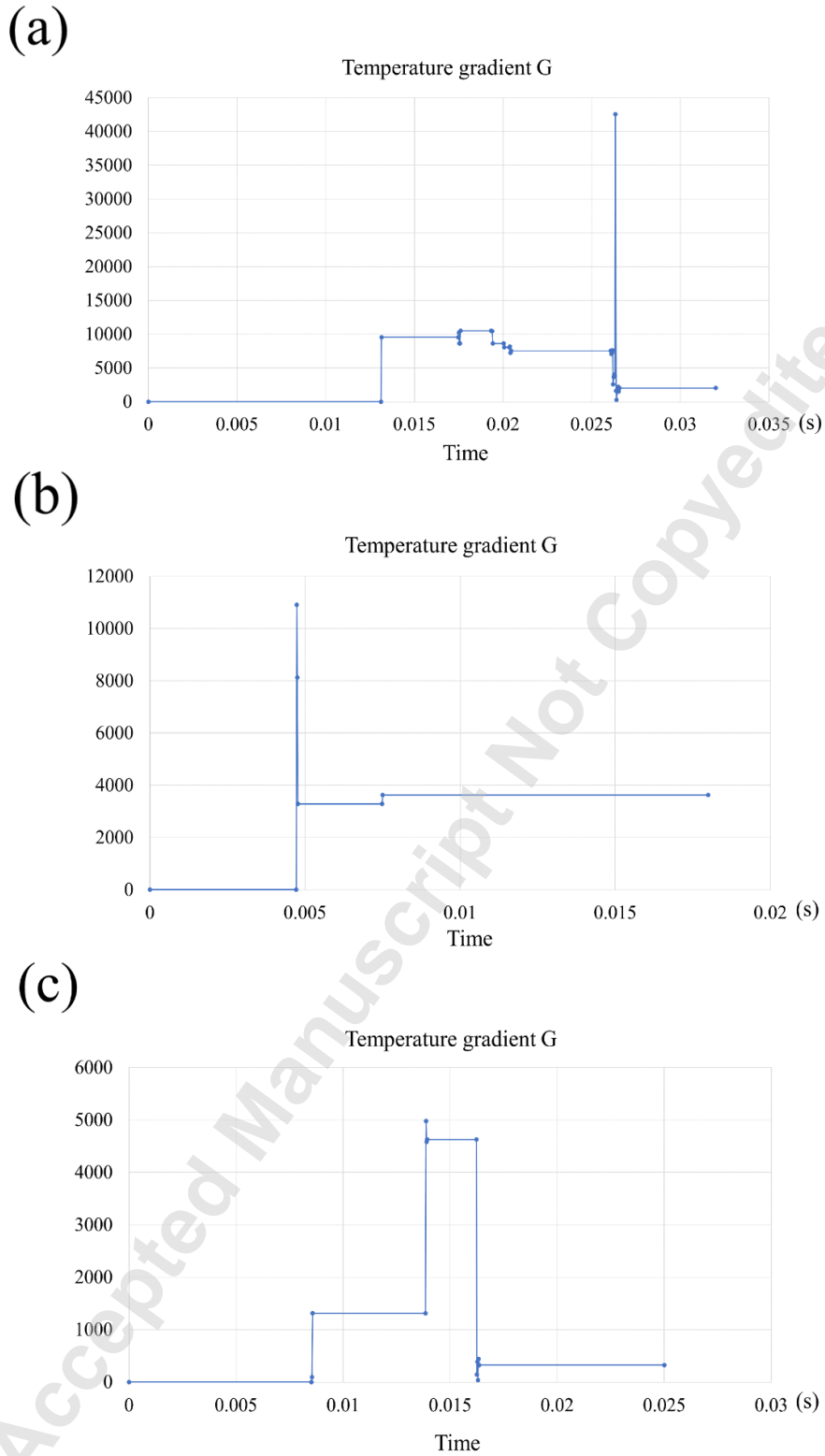
3  
4  
5  
6

Fig. 2 Schematic diagram of the relevant dimensions of each part of the model used in this simulation.

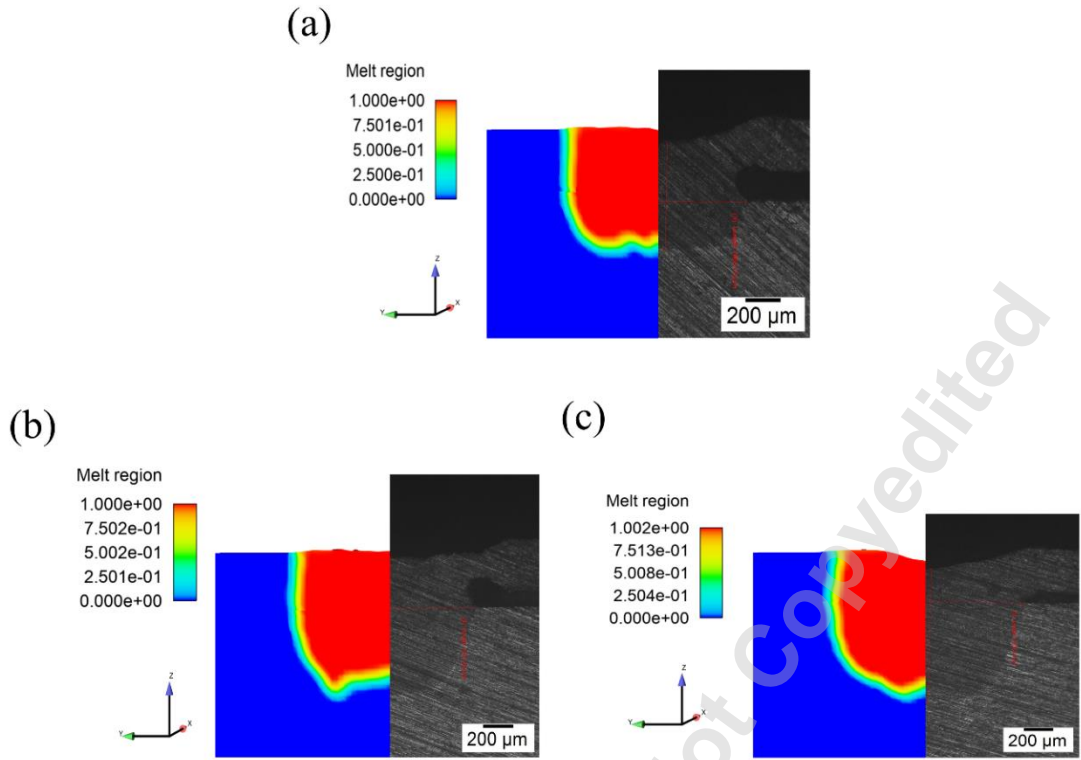


1  
2  
3  
4  
5  
6  
7

Fig. 3 Photos of the upper surface of the weld bead as an experimental result observed with an optical microscope under (a) 600 W – 300 mm/s at the frequency of 136 Hz; (b) 700 W – 350 mm/s at the frequency of 159 Hz; and (c) 800 W – 400 mm/s at the frequency of 182 Hz.

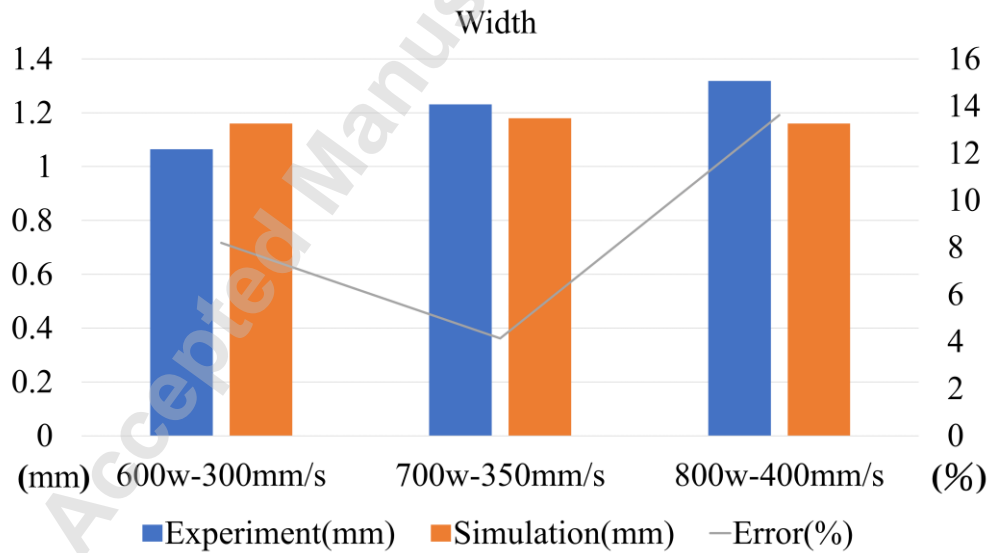


1  
2 Fig. 4 The temperature gradient data derived from the simulation results under (a) 600  
3 W – 300 mm/s at the frequency of 136 Hz; (b) 700 W – 350 mm/s at the frequency of  
4 159 Hz; and (c) 800 W – 400 mm/s at the frequency of 182 Hz.  
5



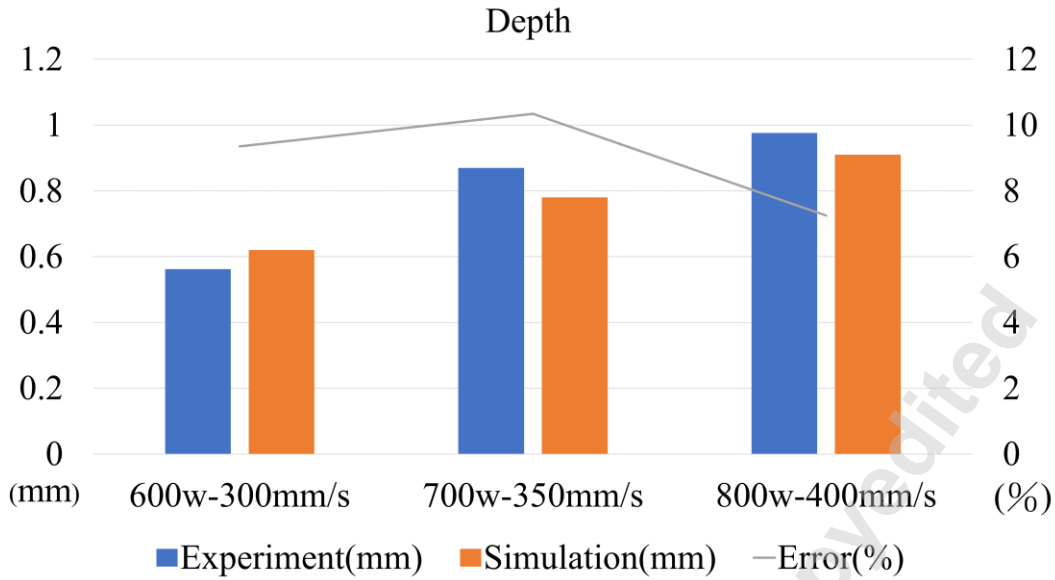
1  
2  
3  
4

Fig. 5 Comparison of experimental and simulated results for each given parameter under (a) 600 W – 300 mm/s at the frequency of 136 Hz; (b) 700 W – 350 mm/s at the frequency of 159 Hz; and (c) 800 W – 400 mm/s at the frequency of 182 Hz.



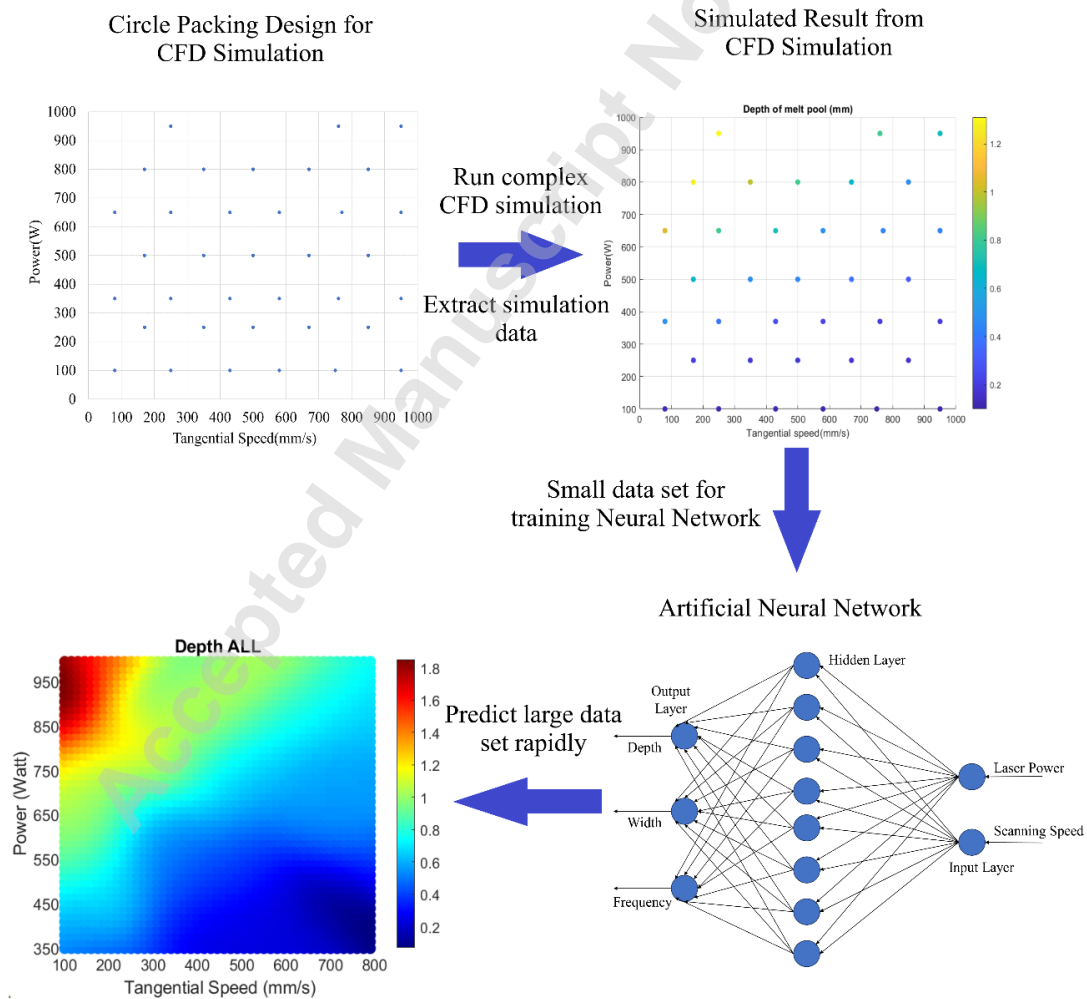
5  
6  
7  
8

Fig. 6 Comparison of the width dimension between the experimental and simulation results for each given parameter.



1  
2  
3

Fig. 7 Comparison of the depth dimension between the experimental and simulation results for each given parameter.

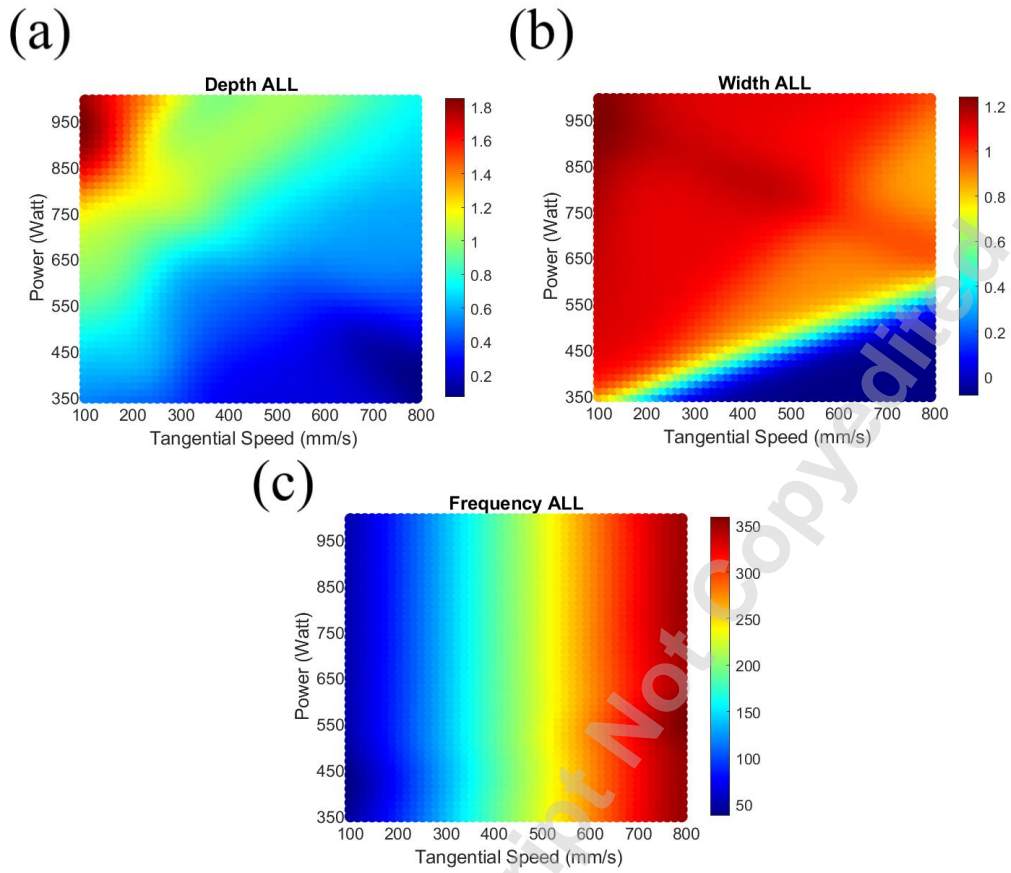


4  
5

Fig. 8 Schematic diagram of the process of using the circle packing design to apply

1

the ANN module to generate processing maps.

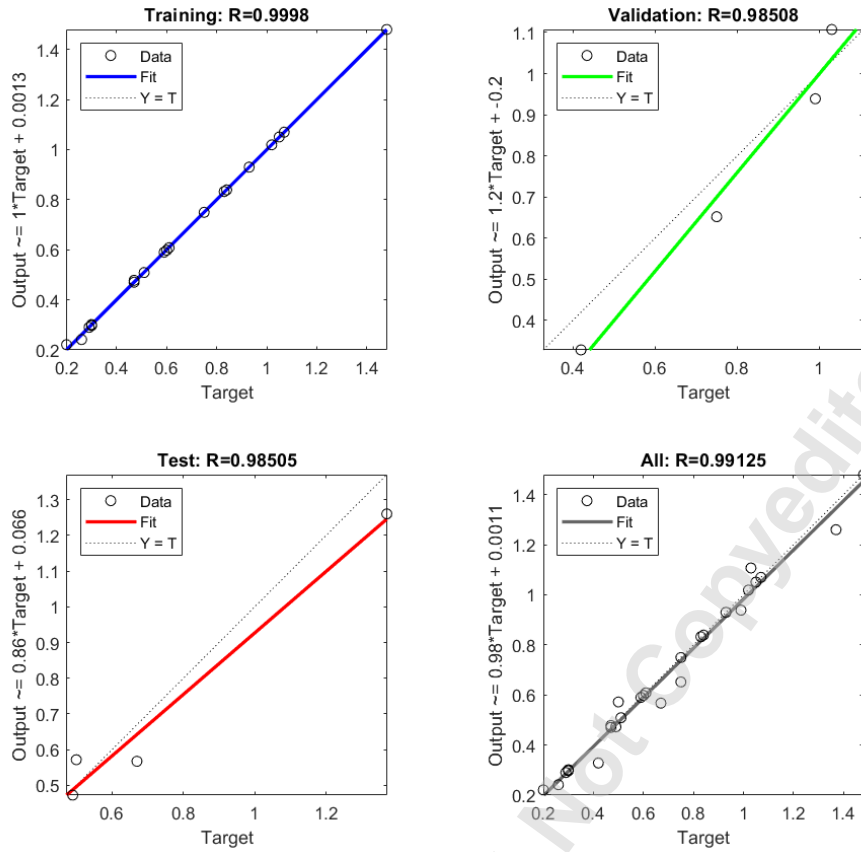


2

3 Fig. 9 Preliminary generation of processing maps for the (a) Depth; (b) Width; and (c)

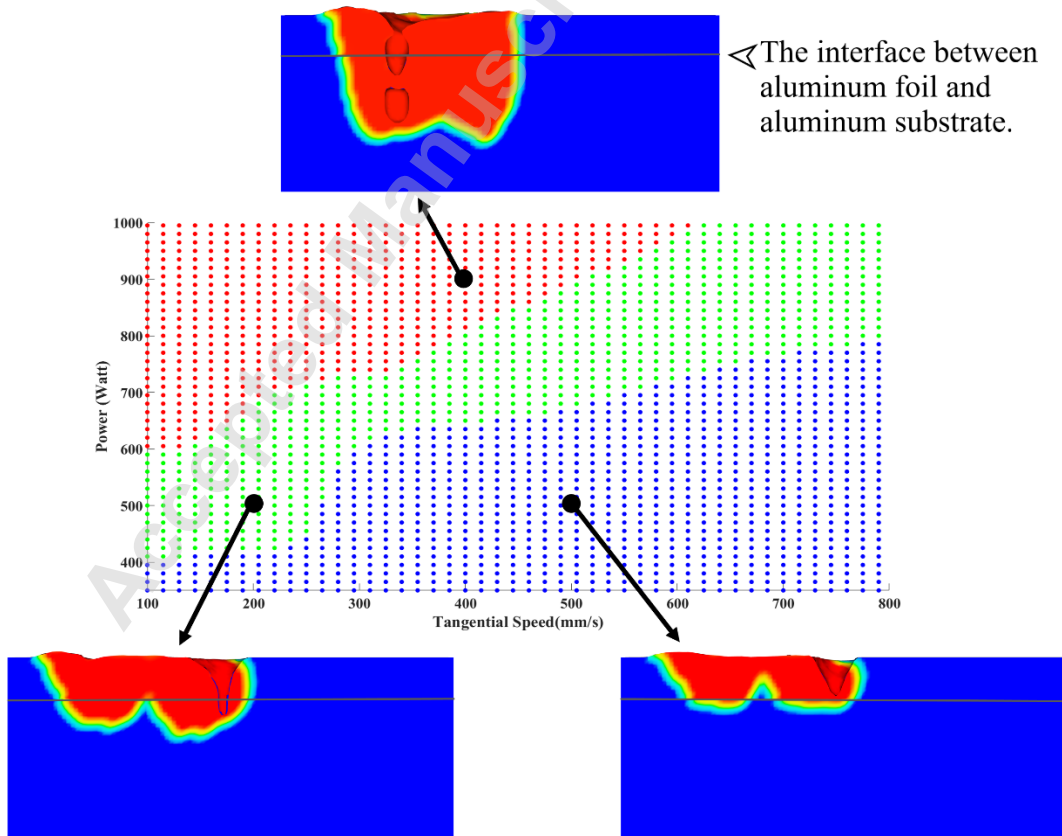
4

Frequency of the weld bead.



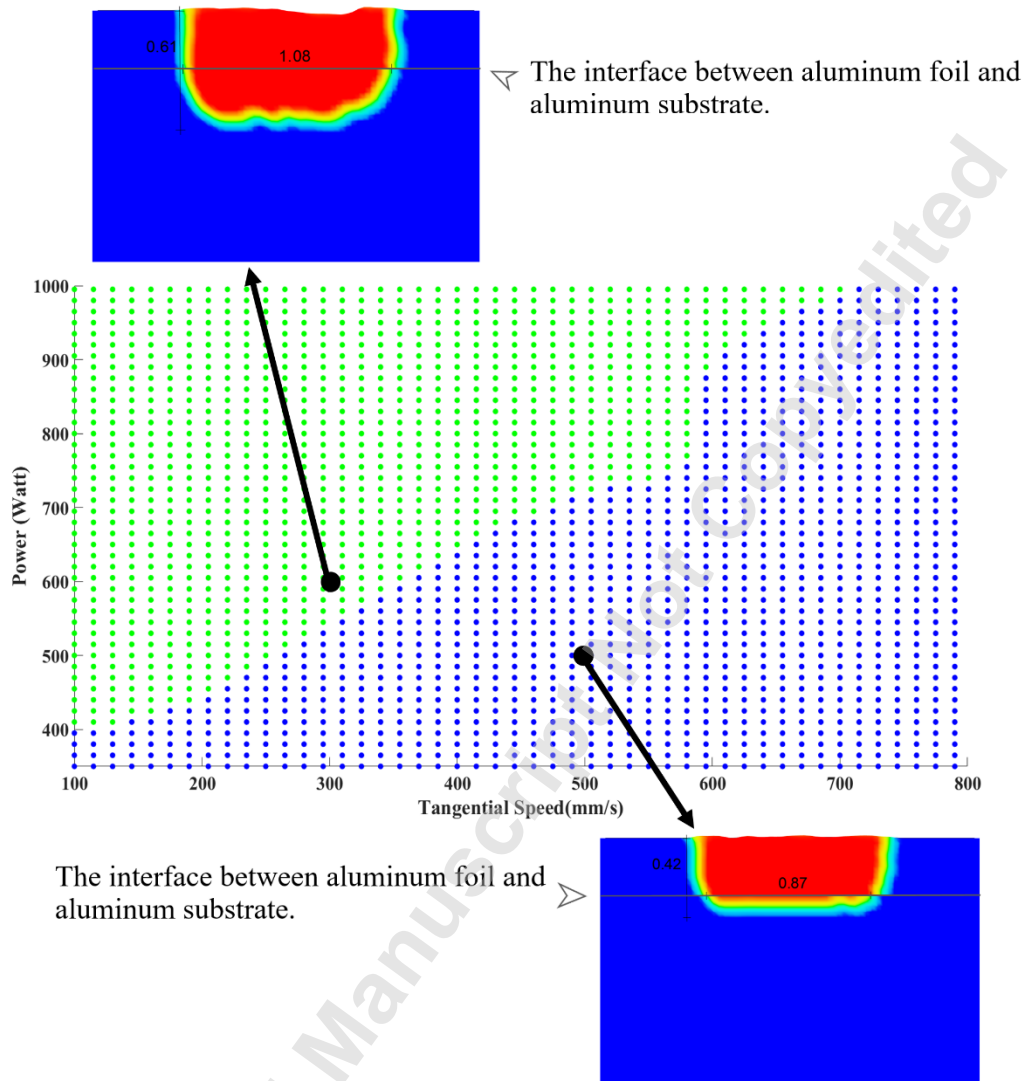
1  
2

Fig. 10 ANN model accuracy results throughout the process.

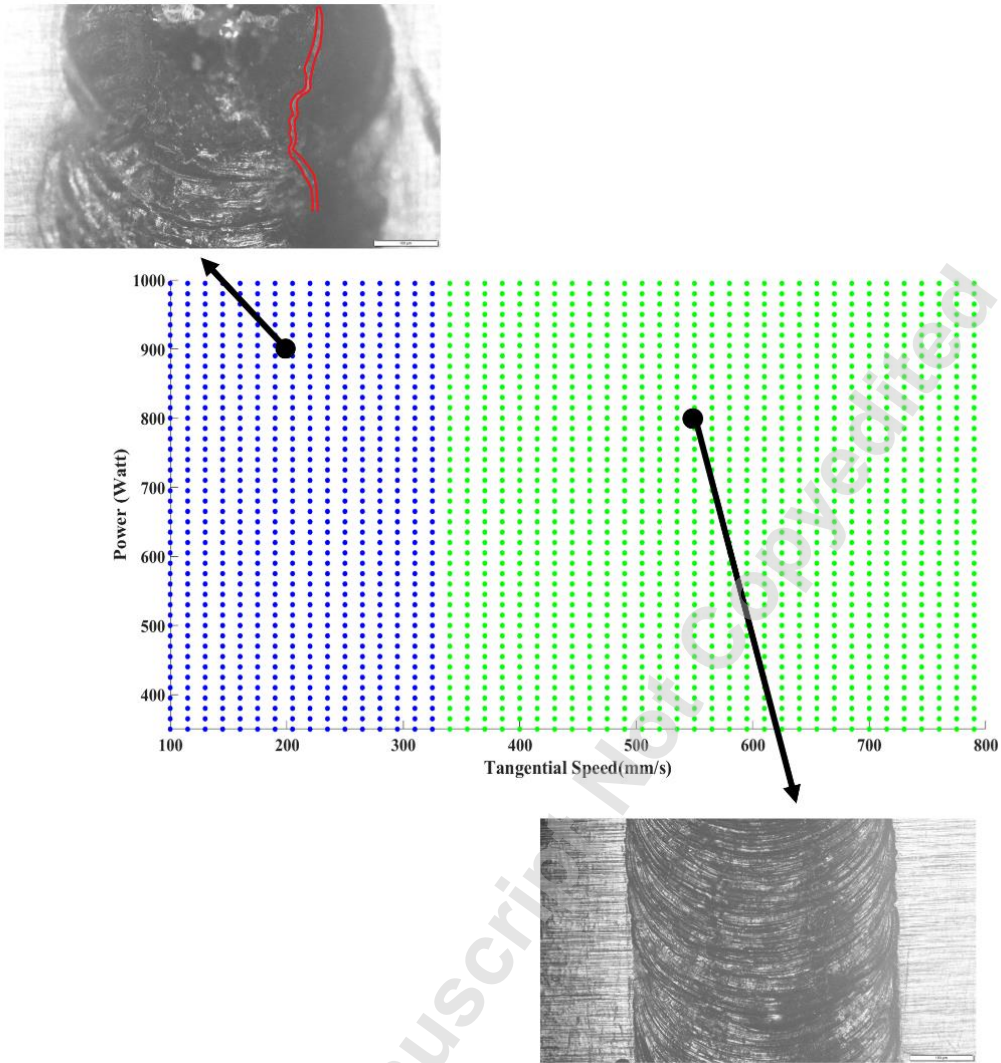


3

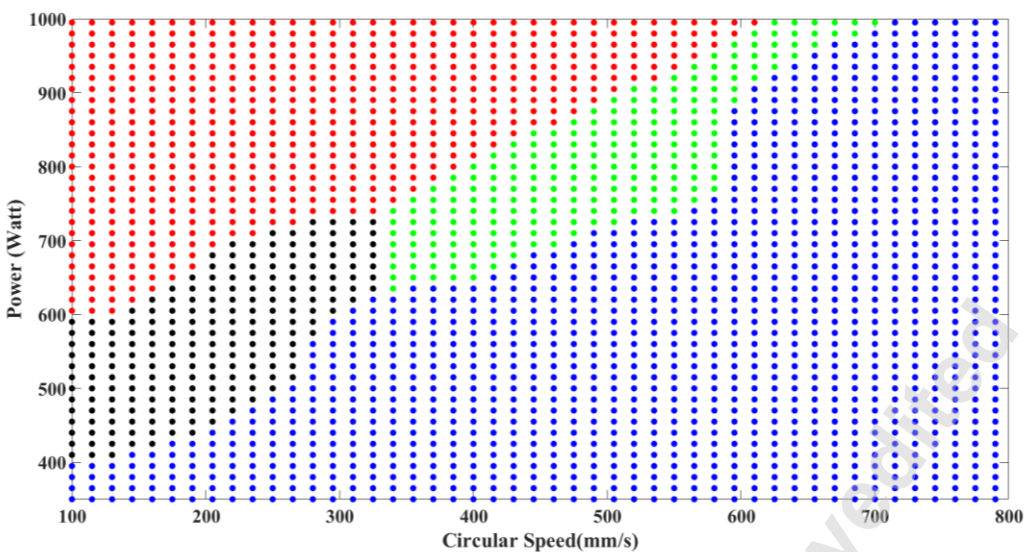
1 Fig. 11 Weld bead depth in the processing map after adding the defined optimal  
2 parameter range.



3  
4 Fig. 12 Weld bead width in the processing map after adding the defined optimal  
5 parameter range.

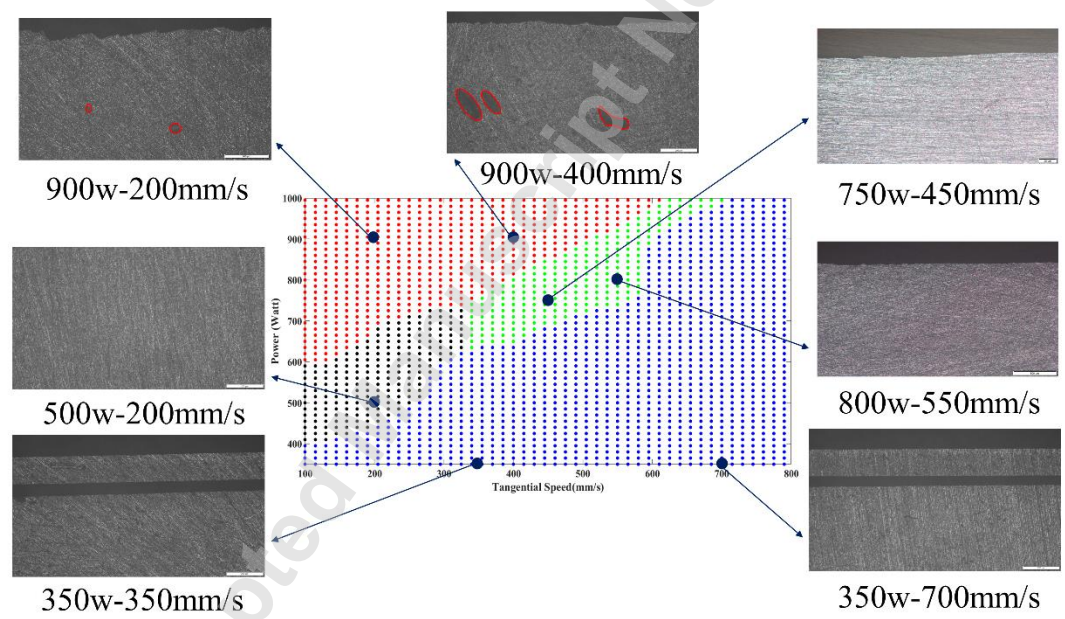


1  
2 Fig. 13 Weld bead frequency in the processing map after adding the defined optimal  
3 parameter range.



1  
2  
3  
4

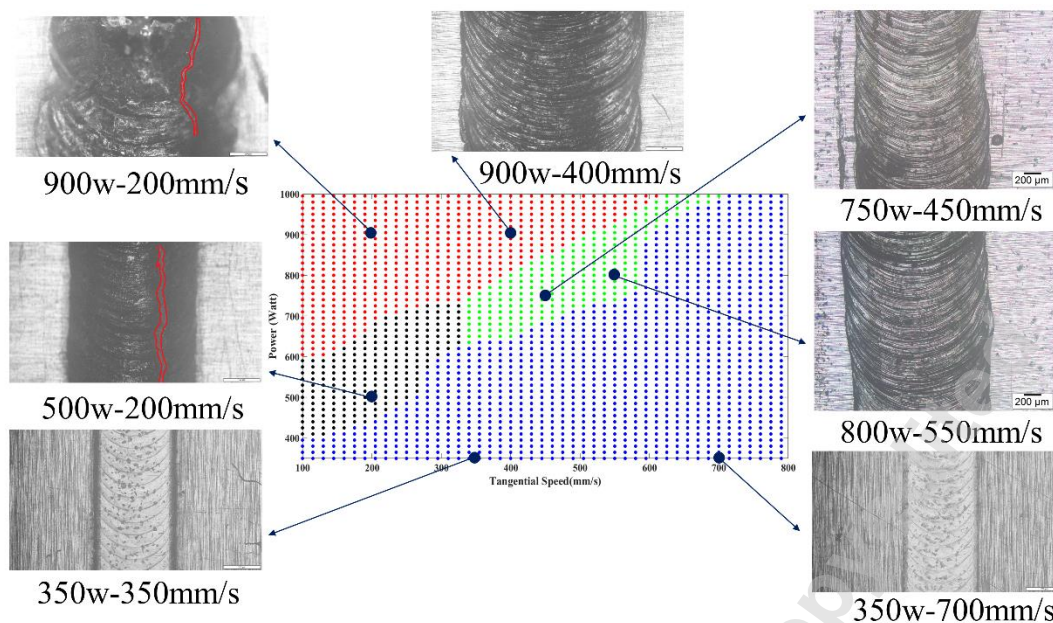
Fig. 14 Optimized depth, width, and frequency range in a processing map after synthesis.



5  
6  
7  
8  
9  
10  
11  
12  
13

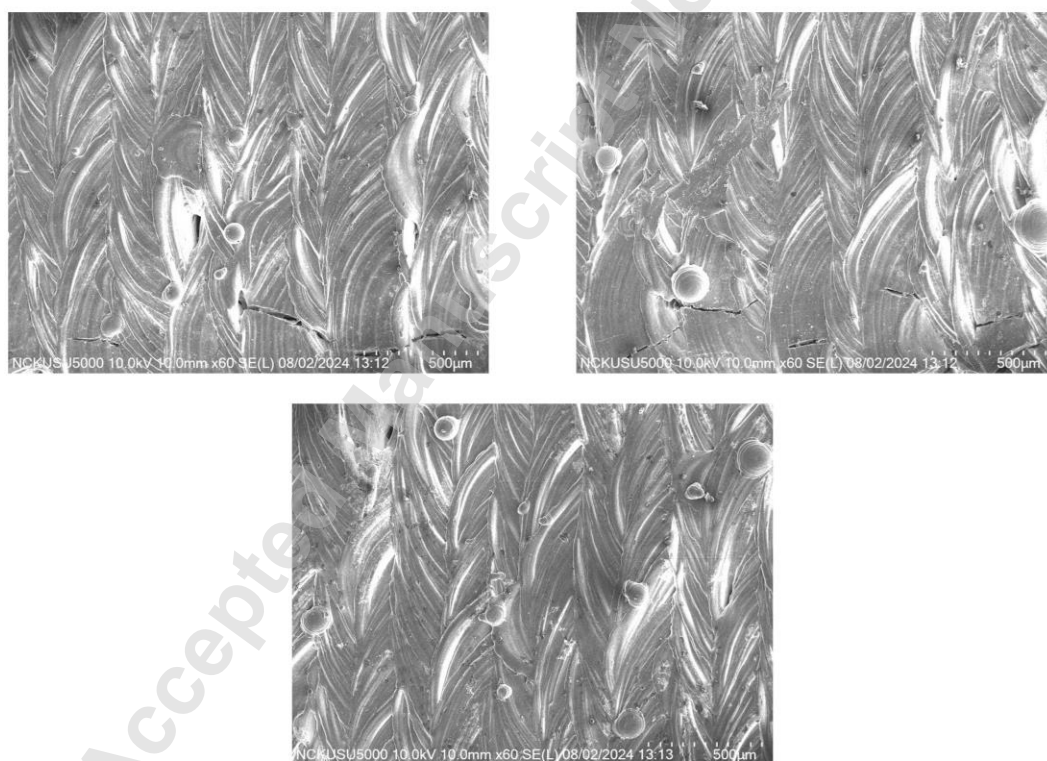
Fig. 15 Experimental results of the longitudinal section of weld bead with processing parameters in each area.

Downloaded from <http://asmmedigitalcollection.asme.org/manufacturingscience/article-pdf/doi/10.1115/1.4066440/7374674/manu-24-1223.pdf> by National Cheng Kung University, Yu-Lung Lo on 09 September 2024



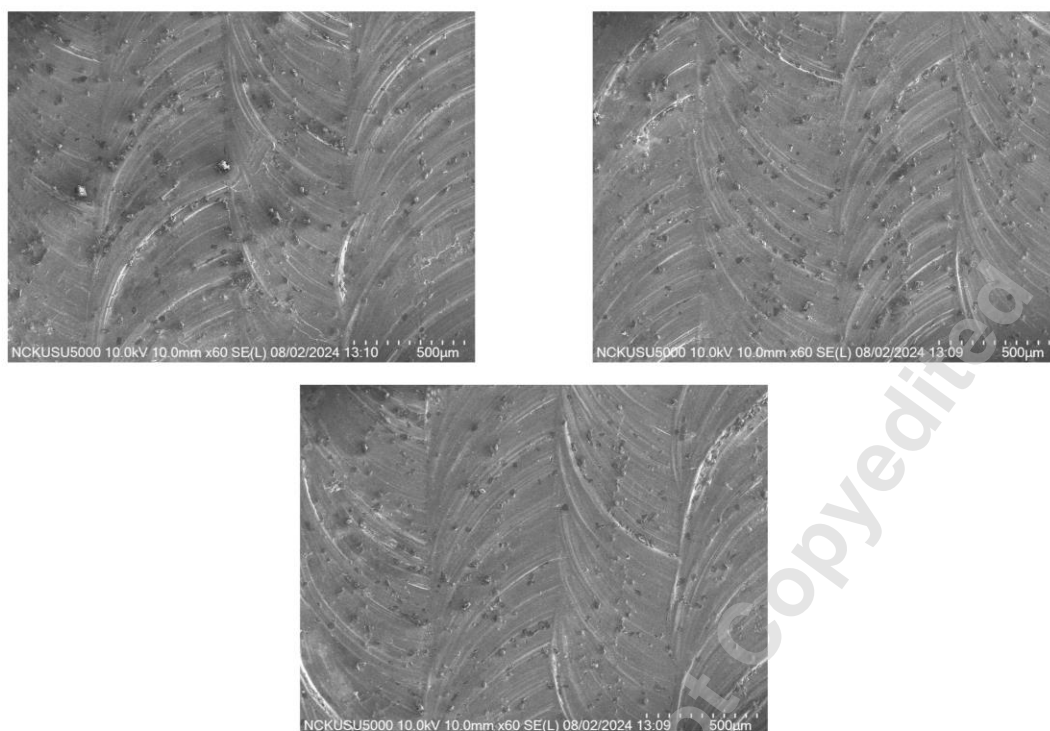
1  
2  
3

Fig. 16 Experimental results on the upper surface of the weld bead with processing parameters in each area.



4  
5  
6  
7  
8

Fig. 17 Experimental results of surface crack distribution on LFP samples using the NOLW strategy.



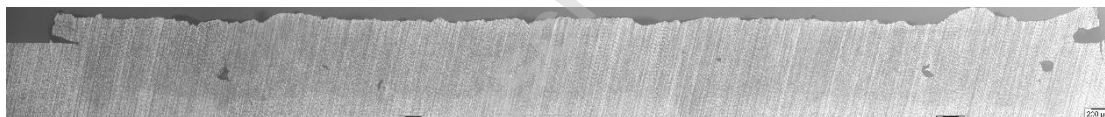
1

2

Fig. 18 Experimental results of surface crack distribution on LFP samples using the  
LCOW strategy.

3

4



5

Fig. 19 Experimental results of pore distribution in the cross-section of LFP samples  
using the NOLW strategy.

6

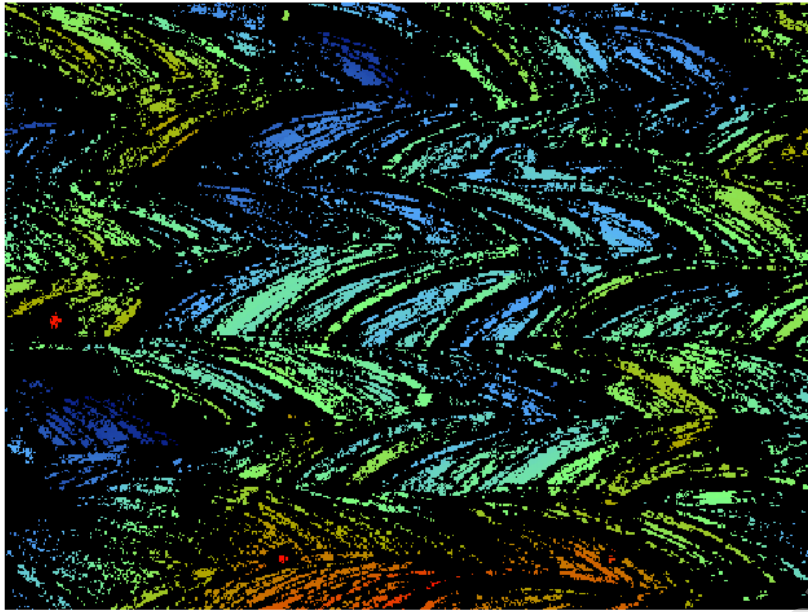
7



8

Fig. 20 Experimental results of pore distribution in the cross-section of LFP samples  
using the LCOW strategy.

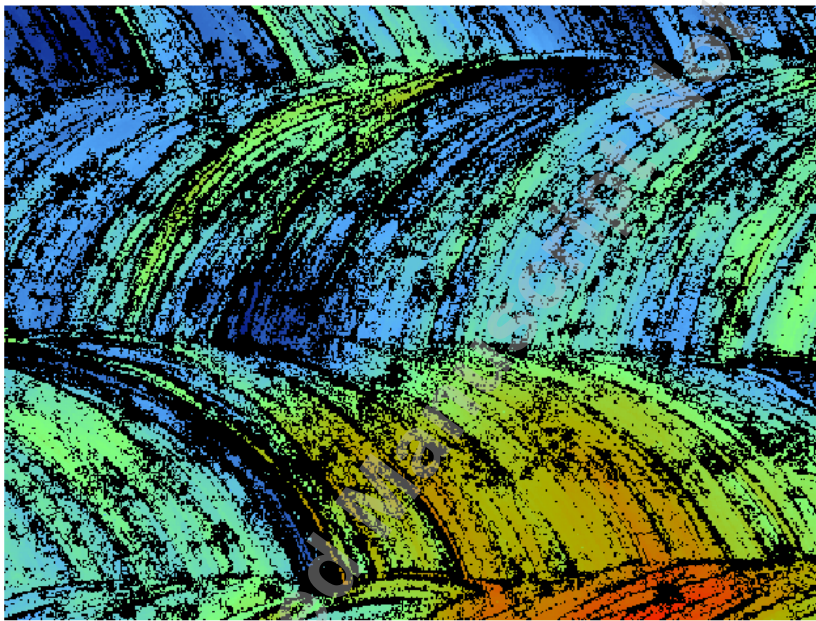
9



Analytical Results		
Label	Value	Units
Sa	20.969	μm
Sku	3.477	
Sp	104.333	μm
Sq	27.174	μm
Ssk	-0.086	
Sv	-97.332	μm
Sz	201.665	μm

1

2 Fig. 21 Surface roughness test results of LFP samples with the NOLW strategy.



Analytical Results		
Label	Value	Units
Sa	6.551	μm
Sku	3.124	
Sp	28.672	μm
Sq	8.168	μm
Ssk	0.043	
Sv	-35.651	μm
Sz	64.323	μm

3

4 Fig. 22 Surface roughness test results of LFP samples with the LCOW strategy.

5

6 **Tables:**

7

Table 1 Relevant parameters used in LCOW.

$A$ (mm)	Power (W)	$V_t$ (mm/s)	$f$ (1/s)	Overlap (%)
0.7	600	300	136	80
0.7	700	350	159	80
0.7	800	400	182	80

1

Table 2 Optimized processing parameters of experimental samples.

	Power (W)	Speed (mm/s)	No. of Layers
NOLW [34]	700	100	5
LCOW	800	550	5

2

Accepted Manuscript Not Copyedited